

Estimation for iron contamination in Si solar cell by ideality factor: deep neural network approach

Oleg Olikh¹ | Oleg Lozitsky¹ | Oleksii Zavhorodnii¹

¹Taras Shevchenko National University of Kyiv, 64/13, Volodymyrska Street, Kyiv, 01601, Ukraine

Correspondence

Olikh O, Taras Shevchenko National University of Kyiv, 64/13, Volodymyrska Street, Kyiv, 01601, Ukraine
Email: olegolikh@knu.ua

Funding information

National Research Foundation of Ukraine, Project Number: 2020.02/0036

Defect-assisted recombination processes frequently limit the photovoltaic device performance. The low-cost and express methods of impurity contamination control are in demand at solar cell manufacturing. In this paper, we applied deep learning-based approach to extract the iron concentration in silicon solar cells from an ideality factor values. SCAPS-1D was the software of choice for the simulation of solar cells with the back surface field design and for the generation of labeled training and test datasets. Our results demonstrated the deep neural network ability to predict iron concentration by using ideality factor values, temperature, and base thickness as well as doping level of a solar cell. The simulation shows that the prediction error is reduced for high doping level, low temperature, and using of two values of ideality factor (for structure with interstitial iron atoms only as well as for structure with coexistence of Fe_i and iron-boron pair). The capability of functioning of the proposed method is verified for real silicon structures.

KEYWORDS

ideality factor, silicon, $n^+ - p - p^+$ structure, iron contamination, SCAPS, machine learning

1 | INTRODUCTION

Metal contamination control remains an important challenge for silicon processing both for microelectronics, logic technologies, and solar cells (SCs) [1, 2, 3, 4]. Typically, metal related defect characterization is performed by Fourier-transform infrared spectroscopy, electron-paramagnetic resonance, minority carrier lifetime measurements, deep level transient spectroscopy (DLTS), Laplace DLTS etc [5, 6, 7]. However, these techniques are time-consuming, require special equipment or/and sample preparation. At the same time, the current-voltage (IV) measurements are the standard rapid industrial SC characterization technique. IV characteristics contain important information about electrically active defects [6, 8]. And several methods are proposed for diagnosing defects using the IV characteristic [6, 8, 9, 10, 11]. The temperature dependencies of current components [10, 11] or IV differential parameters [8, 9] are under consideration. But the numerous and high accuracy IV measurements are required in the first and second cases, respectively.

In our previous work [12], we have shown that the SC ideality factor value (n) can be used to estimate the iron concentration (N_{Fe}). It should be noted that the ideality factor is quite often used to characterize the various semiconductor barrier structures [13, 14, 15, 16, 17]. However, a defect's signature in an ideality factor is convoluted with those from so many other physical processes. As a result, obtained analytic expressions $N_{Fe} = f(n)$ are not general and the numerous grading curves are required to determine N_{Fe} ; besides the IV measurements over a temperature range are necessary [12]. On the other hand, in the last decade, deep learning, which enables solving problems without clear algorithmization, has been successfully used in various fields of theoretical and applied physics [18, 19, 20]. Furthermore, materials informatics (combination of material property calculations/measurements and informatics algorithms) has been asserted [21] to become the fourth (along with theory, simulations, and experiments) paradigm of science. This work aims to apply the deep learning approach for predicting the iron concentration from the ideality factor value (so to say "deep learning for deep levels"). Further, unlike in previous work [12], the back surface field (BSF) $n^+ - p - p^+$ structure was under consideration and the influence of the base thickness on ideality factor was taken into account as well.

As the approximation to the practical using, the paper considers a fairly simple system that consists of crystalline silicon (c-Si) SC and iron impurity. However, the system is important in practice. Silicon solar cells constitute 90% of current global production capacity [22] and BSF is one of the popular designs used for industrial mass production of c-Si SCs as yet [23, 24]. Surely, the passivated emitter and rear cell technology has recently come to the fore, but PERC solar cells contain $n^+ - p$ junction as well [24, 25]. Iron is a major as well as one of the most detrimental metallic impurities in c-Si SCs [2, 3, 4]. The flowchart of the used heuristic approach is shown in Fig. 1. The following constituents can be marked out. First, the dark IV characteristics are simulated for SCs with known contaminant composition and various parameters. In our numerical simulation we applied SCAPS-1D [26, 27], which widely used to model solar cells [28, 29, 30, 31, 32, 33]. Second, the obtained IV curves are fitted according to the double-diode model and the ideality factors are estimated. As a result of the aforesaid steps, the labeled datasets were produced. Obviously, the labeled dataset from experimental IVs would be preferable, but it is practically difficult to find the thousands of samples with the required parameters. Third, the training of deep neural network (DNN) to estimate iron contamination by using SC's base thickness, doping level, temperature, and ideality factor value. Fours, the DNN testing by using synthetic IV curves as well as experimental IV curves.

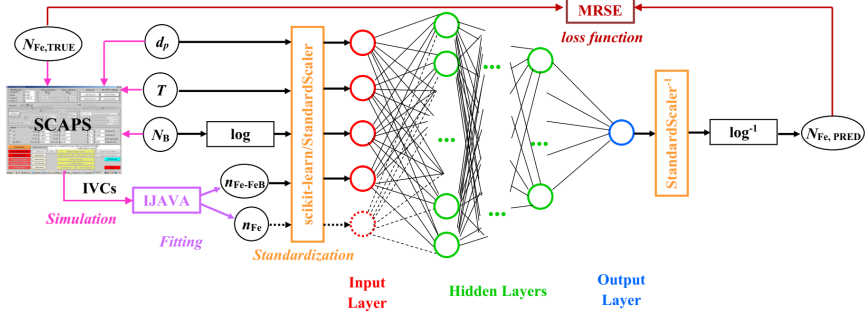


FIGURE 1 Schematic of deep learning-based approach for predicting the iron concentration. Additional details are discussed in the body of the article.

2 | SIMULATION DETAILS

The presented calculation uses $n^+ - p - p^+$ structure: the emitter layer n^+ with the donor concentration $N_D = 10^{19} \text{ cm}^{-3}$ and the thickness $0.5 \mu\text{m}$; p and p^+ are uniformly doped with boron; the base p with the thickness $d_p = 150\text{--}240 \mu\text{m}$ is doped with concentration $N_B = 10^{15}\text{--}10^{17} \text{ cm}^{-3}$ and the BSF-layer p^+ with the thickness d_{BSF} ($1 \mu\text{m}$) and the acceptor concentration N_{BSF} ($5 \times 10^{18} \text{ cm}^{-3}$).

The simulations were carried out over the temperature range $290\text{--}340 \text{ K}$. The SCAPS setting file was created for each temperature using the following material parameters. The bandgap E_G and bandgap narrowing ΔE_G models are, respectively, from Pässler [34] and Yan and Cuevas [35]:

$$E_G = E_{G0} - \alpha\Theta \left\{ \frac{1 - 3\Delta^2}{e^{\frac{\Theta}{T}} - 1} + \frac{3\Delta^2}{2} \left(\sqrt[6]{1 + \frac{\pi^2}{3(1+\Delta^2)} \left(\frac{2T}{\Theta} \right)^2} + \frac{3\Delta^2 - 1}{4} \left(\frac{2T}{\Theta} \right)^3 + \frac{8}{3} \left(\frac{2T}{\Theta} \right)^4 + \left(\frac{2T}{\Theta} \right)^6 - 1 \right) \right\}, \quad (1)$$

$$\Delta E_G = 4.20 \times 10^{-5} \left[\ln \left(\frac{N_D}{10^{14}} \right) \right]^3; \quad \Delta E_G = 4.72 \times 10^{-5} \left[\ln \left(\frac{N_{B,BSF}}{10^{14}} \right) \right]^3, \quad (2)$$

where $E_{G0} = 1.1701 \text{ eV}$, $\alpha = 3.23 \times 10^{-4} \text{ eV/K}$, $\Theta = 446 \text{ K}$, $\Delta = 0.51$. The carrier thermal velocities are calculated from models by Green [36]:

$$v_{th,n} = \sqrt{\frac{8qkT}{0.28m_0\pi}}; \quad v_{th,p} = \sqrt{\frac{8qkT}{0.41m_0\pi}}, \quad (3)$$

where m_0 is the free electron mass. The effective states density masses in the conduction band m_{dC}^* and the valence band m_{dV}^* are calculated according to models from Couderc et al. [37]:

$$\left(\frac{m_{dC}^*}{m_0} \right)^{1.5} = 1.094 - 1.312 \times 10^{-5}T + 6.753 \times 10^{-7}T^2 + 4.609 \times 10^{-10}T^3, \quad (4)$$

$$\left(\frac{m_{dV}^*}{m_0} \right)^{1.5} = 0.3426 + 3.376 \times 10^{-3}T - 4.689 \times 10^{-6}T^2 + 2.525 \times 10^{-9}T^3. \quad (5)$$

The carrier mobilities and the free carrier effective masses were taken from Klaassen [38] and O'Mara et al. [39], respectively. The temperature and doping dependencies of Auger recombination coefficients are calculated from

models by Altermatt et al. [40]:

$$C_p(T) = (7.91 \times 10^{-32} - 4.13 \times 10^{-35} T + 3.59 \times 10^{-37} T^2) \times \left(1 + (564812 T^{-1.6545} - 1) \left(1 - \tanh \left[\left\{ \frac{p}{5 \times 10^{16}} \right\}^{0.29} \right] \right) \right), \quad (6)$$

$$C_n(T) = 2.8 \times 10^{-31} \times \left(1 + (235548 T^{-1.5013} - 1) \left(1 - \tanh \left[\left\{ \frac{n}{5 \times 10^{16}} \right\}^{0.34} \right] \right) \right). \quad (7)$$

The band-to-band radiation recombination coefficient was taken from Nguyen et al. [41].

The outside surface recombination with electron and hole velocities 10^3 cm/s was taken into account.

The simulations are carried out under the assumption that the defect-assisted recombination corresponds to the iron-related deep levels only. As the base and the SBF-layer uniform contaminant, iron is assumed to be in concentration $N_{Fe} = 10^{10} - 10^{13}$ cm⁻³. The simulations have been performed for the following two cases. In the first one, the concentration of total dissolved iron is given by a sum of concentrations of the interstitial iron Fe_i and the trigonal iron-boron pair Fe_iB_s :

$$N_{Fe} = N_{Fe_i} + N_{Fe_iB_s}. \quad (8)$$

The defect distributions are inhomogeneous, and depend on the Fermi level F position, and are given by [42, 43]:

$$\frac{N_{FeB}}{N_{Fe}} = \frac{N_B 10^{-23} \exp\left(-\frac{E_b}{kT}\right)}{\left[1 + \frac{N_B}{10^{23}} \exp\left(-\frac{E_b}{kT}\right)\right] \left[1 + \exp\left(-\frac{F - E_{Fe_i}}{kT}\right)\right]}, \quad N_{Fe_i} = N_{Fe} - N_{FeB}, \quad (9)$$

where $E_b = 0.582$ eV is the binding energy of the Fe_iB_s pairs, E_{Fe_i} is the donor level, associated with Fe_i . This case corresponds to the equilibrium condition and in this article will be referred to as “Fe-FeB”.

In the second one, the Fe_i is suggested to be presented only with homogeneous distribution ($N_{Fe_i} = N_{Fe}$). This case can be realized by heat treatment (210°C, 3 min) [44] or intense illumination [45] and will be referred as “Fe” hereafter.

The donor level $E_{Fe_i} = E_V + 0.394$ eV with electron $\sigma_{n,Fe} = 3.47 \times 10^{-11} T^{-1.48}$ cm² and hole $\sigma_{p,Fe} = 4.54 \times 10^{-16} \exp\left(-\frac{0.05}{kT}\right)$ cm² capture cross-sections [42, 46] is associated with Fe_i in simulations. The donor level $E_{FeB}^D = E_V + 0.10$ eV, $\sigma_{n,FeB}^D = 4 \times 10^{-13}$ cm², $\sigma_{p,FeB}^D = 2 \times 10^{-14}$ cm² and acceptor level $E_{FeB}^A = E_C - 0.26$ eV, $\sigma_{n,FeB}^A = 5.1 \times 10^{-9} T^{-2.5}$ cm², $\sigma_{p,FeB}^A = 3.32 \times 10^{-10} \exp\left(-\frac{0.262}{kT}\right)$ cm² [47, 42, 46] are used for Fe_iB_s .

The dark forward IV characteristics were generated by SCAPS over a voltage range up to 0.45 V. According to the two-diode model, the dark SC current is given by [48]

$$I = I_{01} \left[\exp\left(-\frac{q(V - R_s I)}{kT}\right) - 1 \right] + I_{02} \left[\exp\left(-\frac{q(V - R_s I)}{nkT}\right) - 1 \right] + \frac{V - R_s I}{R_{sh}}, \quad (10)$$

where I_{01} and I_{02} are the saturation currents, R_{sh} and R_s are the shunt and series resistances. The two-diode model is often applied for description of real Si SCs and the first diode represents the “ideal” diode and first term in Eq. (10) current is due to recombination in the base and the emitter, including their surfaces; the second diode is the so-called recombination diode and first term is due to recombination within the depletion region [48].

and we used Eq. (10) to fit the simulated data by taking n , I_{01} , I_{02} , R_{sh} , and R_s as fitting parameters. The fitting was performed by using the meta-heuristic method IJAVA [49]. It should be noted that influence of both R_s (obtained values $< 10^{-2}$ Ω) and R_{sh} (obtained values $> 10^{18}$ Ω) can be neglected in simulated IV.

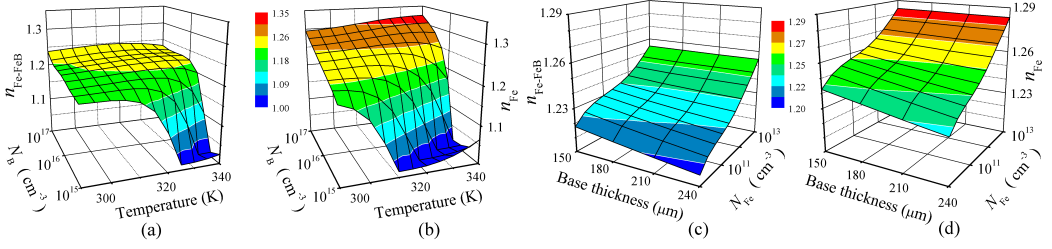


FIGURE 2 Ideality factor versus temperature and boron concentration (a, b) or base thickness and iron concentration (c, d). The Fe-FeB-case (a, c) and Fe-case (b, d). $N_{Fe} = 10^{10} \text{ cm}^{-3}$ (a, b), $d_p = 180 \mu\text{m}$ (a, b), $N_B = 10^{16} \text{ cm}^{-3}$ (c, d), $T = 320 \text{ K}$ (c, d).

It is the ideality factor value n which is used in our further calculation. The ideality factors, which are obtained in Fe-case and Fe-FeB-case, are referred to as n_{Fe} and n_{Fe-FeB} hereafter. The typical simulated dependencies of the ideality factor are shown in Fig. 2. The detailed discussion about n_{Fe} and n_{Fe-FeB} values are presented elsewhere [50], however it should be noted that (i) n can take equal values for different values of SC parameters; (ii) dependencies of n_{Fe} and n_{Fe-FeB} vary not only in absolute values but although in behavior slightly.

3 | DEEP NEURAL NETWORK MODELS

Training a deep neural network requires a large number of samples. In order to build a training dataset, we used IV characteristics, which are simulated with using of 4 d_p values, 9 N_B values, 11 T values and 19 N_{Fe} values. These base thickness, doping level, temperature, and iron concentration values are regularly (for T and d_p in linear scale, for N_{Fe} and N_B in logarithmic scale) distributed over the ranges 150–240 μm , 10^{15} – 10^{17} cm^{-3} , 290 – 340 K, and 10^{10} – 10^{13} cm^{-3} , respectively. Thus, 7524 IV characteristics are simulated in Fe-case as well as in Fe-FeB-case to build a training dataset.

Besides, several test datasets are prepared. The d_p , N_B , and N_{Fe} values, which equal to values from training dataset, and T values, which is divergent from training dataset, are used to build the test dataset, labeled “T-varied”. This dataset is based on 894 pairs of IV characteristics. The similar approach was used to prepare “d-varied” (1189 samples), “Fe-varied” (856 samples), and “B-varied” (514 samples) test datasets. The base thickness, doping level, temperature, and iron concentration values, which are divergent from training dataset values, are used to prepare “All-varied” (684 samples).

The precise values of parameters are listed in Supplementary Material.

We have tried to construct the DNN, which can estimate iron contamination by using SC parameters (d_p and N_B), measurement temperature, and the result of IV fitting (ideality factor value). As it is shown in Fig. 1 two DNNs with different input parameters were under consideration. The input sample of the first one consist of $\{d_p, \log N_B, T, n_{Fe-FeB}\}$. In practice, this input set can be obtained from one dark IV measurement. This neural network is referred to as DNN_{FeFeB} hereafter. The second one uses $\{d_p, \log N_B, T, n_{Fe-FeB}, n_{Fe}\}$ in input layer. In practice, the obtaining of such a set requires additional SC processing (e.g., intense illumination) and two IV measurements. The label $\text{DNN}_{FeFeB-Fe}$ is used below.

The dense deep neural network was implemented through the high-level Keras API provided by TensorFlow [51]. The input layers consist of 4 or 5 nodes — see Fig. 1. 1 node and linear activation were used in the output layer. The five configurations of hidden layers were under consideration: (i) “pipe”: each hidden layer contains equal number of nodes; (ii) “trapezium”: six hidden layers, number of neurons linearly decreases from 100% (first layer) to 50% (last layer);

TABLE 1 Hyperparameter space for DNNs.

Hyperparameter	Values
# nodes for first hidden layer	30, 40, 50, 75, 100, 120, 150
# hidden layers	4, 5, 6, 8, 10, 15
batch size	8, 16, 32, 64, 128
activation function	ReLu, sigmoid, tanh, SELU, ELU
optimizer	SGD, RMSprop, Adam, Adadelta, Adagrad, Adamax, Nadam, Ftrl
learning rate	10^{-5} , 10^{-4} , 10^{-3} , 10^{-2}
# epochs	100, 300, 400, 600, 1000, 1500
preprocessing method	StandartScaler, MinMaxScaler
regularization function	None, L2, L1, Dropout
regularization rate	10^{-5} , 10^{-4} , 10^{-3} , 10^{-2}
dropout rate	0.2, 0.3, 0.4, 0.5
weight initializer	Xavier Normal or Uniform, He Normal or Uniform, Random Normal or Uniform, Ones

(iii) “triangle”: ten layers, number of neurons linearly decreases from 100% (first layer) to 10% (last layer); (iv) “butterfly”: two serial reflected trapezium configurations; (v) “fir”: two serial trapezium configurations.

The mean squared relative error (MSRE) was chosen as the loss function:

$$\text{MSRE} = \frac{1}{N_s} \sum_{i=1}^{N_s} \frac{(N_{\text{Fe,TRUE},i} - N_{\text{Fe,PRED},i})^2}{N_{\text{Fe,TRUE},i} \cdot N_{\text{Fe,PRED},i}}, \quad (11)$$

where N_s is the number of samples in dataset, $N_{\text{Fe,TRUE},i}$ is the iron concentration, which was used in simulation of i -th sample, $N_{\text{Fe,PRED},i}$ is the DNN prediction for i -th sample.

Hyperparameters include the number of nodes for the first hidden layer, the number of hidden layers (in pipe configuration), the batch size, the activation function, the optimizer, the learning rate, the preprocessing method, the dropout rate, the regularization function, the regularization rate, and the weight initializer. A grid search (coarse tuning to limit one hyperparameter) and random search (fine tuning) were performed over the predefined hyperparameter space, shown in Table 1, and the best hyperparameter combination is chosen.

10-fold cross-validation was used to estimate DNN training. The MSRE, coefficient of determination R^2 , and coefficient of correlation R were three metrics used to evaluate the performance of the DNN models on test datasets. Finally, to increase a DNNs performance, the full dataset, which consists of training dataset and all test datasets, was used for the training models.

TABLE 2 Chosen hyperparameter combinations.

Hyperparameter	$\text{DNN}_{\text{FeFeB}}$	$\text{DNN}_{\text{FeFeB-Fe}}$
# nodes for hidden layers	120, 108, 96, 84, 72, 60	100, 100, 100, 100
batch size	32	32
activation function	ReLU	ELU
optimizer	Adamax	Adamax
learning rate	10^{-3}	10^{-3}
# epochs	400	1500
preprocessing method	StandartScaler	StandartScaler
regularization function	None	None
weight initializer	Xavier Normal	Xavier Normal

TABLE 3 Results of 10-fold cross-validation

Dataset	MSRE	
	$\text{DNN}_{\text{FeFeB}}$	$\text{DNN}_{\text{FeFeB-Fe}}$
training	0.31 ± 0.07	0.03 ± 0.01
full	0.28 ± 0.05	0.03 ± 0.01

4 | RESULTS AND DISCUSSION

4.1 | Synthetic IV curves

The results of the hyperparameter search are listed in Table 2. In particular, the trapezium and pipe configurations are chosen for $\text{DNN}_{\text{FeFeB}}$ and $\text{DNN}_{\text{FeFeB-Fe}}$ respectively.

The training and test results of $\text{DNN}_{\text{FeFeB}}$ are presented in Table 3, Table 4, and Fig. 3. As we can see, that MSRE of $\text{DNN}_{\text{FeFeB}}$ prediction is sufficiently large. But it should be noted, that the fraction of prediction with a big difference between $N_{\text{Fe,TRUE},i}$ and $N_{\text{Fe,PRED},i}$ is not numerous in most cases. Thus squared relative error (SRE) does not exceed 0.05 for 87%, 88%, and 96% samples from T-varied, d-varied and Fe-varid datasets respectively – see bars in Fig. 3. For the B-varied dataset (with doping level value, non-used in the training dataset) the biggest MSRE = 1.06 connects to the occurrence of some samples with a really big SRE (>20). While SRE is less than 0.05 in 54% of samples from the B-varied test dataset. The worst predictions are quite expectedly to be observed for the All-varied dataset: R^2 equals 0.813 and SRE is less than 0.05 for 18% only. On the other hand, the Fe-varied dataset is most similar to real demand. And determination and correlation coefficients are high enough (0.991 and 0.996) in this case.

The dependencies on DNN prediction error on SC parameters values are under consideration too – see Figs. 4– 7. These figures represent data for the training dataset, the results for test datasets are similar. Thus Fig. 4(a) shows that the considerable increase in prediction error value is observed at $T > 320$ K for $\text{DNN}_{\text{FeFeB}}$. So the maximum SRE is about 20 and the SRE is less than 0.01 for 55% of samples at $T = 340$ K (Fig. 4(c)). Whereas those values are equal to 0.02 and 83% at $T = 290$ K (Fig. 4(b)). It has been shown previously [50], that temperature rise causes the increase in the intrinsic recombination's contribution to an ideality factor. As a result, the sign of Shockley-Read-Hall (SRH)

TABLE 4 DNN's testing results

Dataset	DNN _{FeFeB}			DNN _{FeFeB-Fe}		
	MSRE	R^2	R	MSRE	R^2	R
T-varied	0.41	0.936	0.967	0.020	0.994	0.997
d-varied	0.37	0.961	0.980	0.018	0.996	0.998
B-varied	1.06	0.881	0.939	0.084	0.991	0.995
Fe-varied	0.06	0.991	0.996	0.005	0.999	0.999
All-varied	0.54	0.813	0.901	0.138	0.948	0.974

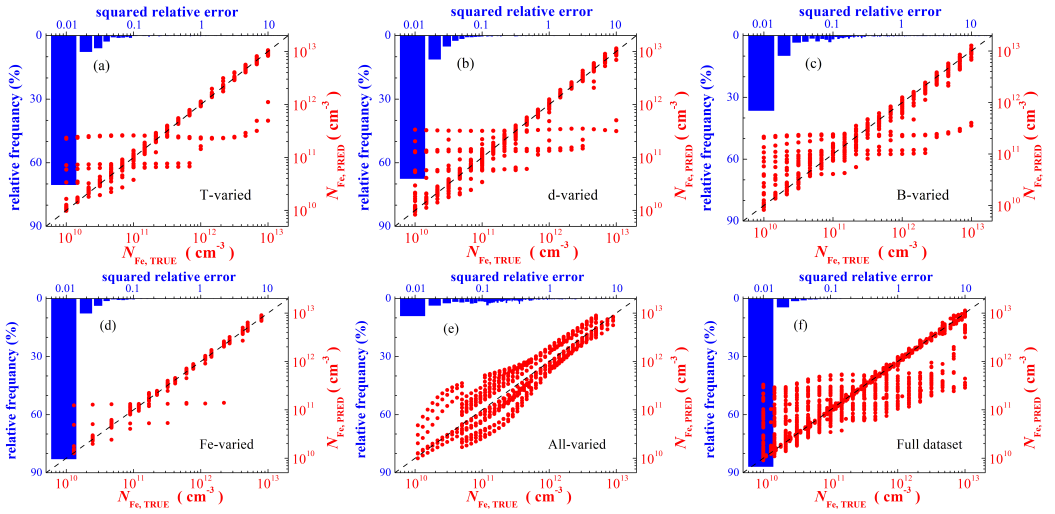


FIGURE 3 Iron concentrations are plotted against those generated by DNN_{FeFeB} on T-varied (a), d-varied (b), B-varied (c), Fe-varied (d), All-varied (e), and full (f) datasets (red points). Bars represent histograms of squared relative error. DNN was learned by training (a)–(e) or full (f) dataset. The black dashed lines are the identify lines serving as the references.

recombination in n value become less evident and DNN predictive ability falls.

As shown in Fig. 5, the SC base thickness does not influence the prediction error (mean value as well as relative frequency) practically. But one can see in Fig 2(c,d), that an ideality factor value depend on base thickness at constant N_{Fe} . Therefore d_p is a significant parameter for DNN training.

The predictive error rises sharply with doping level decrees — see Fig. 6(a). Thus maximum SRE is about 0.05 for $N_B = 10^{17} \text{ cm}^{-3}$ (Fig. 6(c)) whereas squared relative error is less than 0.05 for 56% of samples only for $N_B = 10^{15} \text{ cm}^{-3}$ (Fig. 6(b)). The hole occupation of the Fe-related level determines the SRH recombination efficiency. Accordingly to the Fermi-Dirac statistics, the probability of a hole occupation in a non-degenerate p -type semiconductor with full acceptor

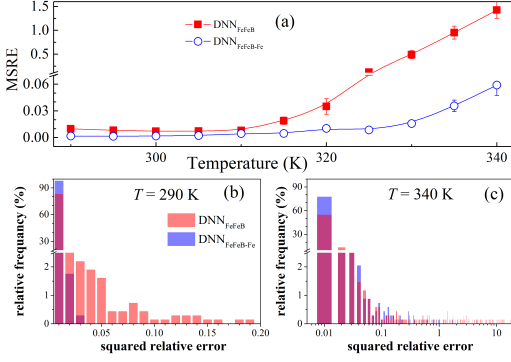


FIGURE 4 (a) Dependence of the MSRE (training dataset) on the temperature. (b),(c) Histograms of squared relative error for $T = 290$ K and $T = 340$ K. Red: $\text{DNN}_{\text{FeFeB}}$; blue: $\text{DNN}_{\text{FeFeB-Fe}}$.

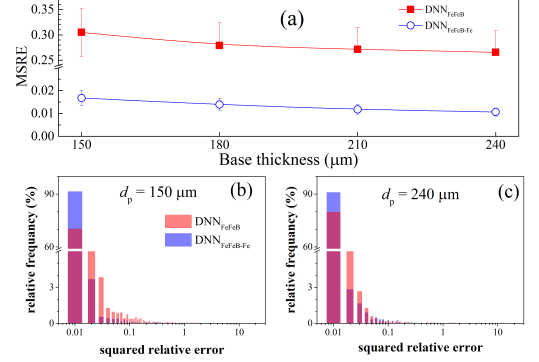


FIGURE 5 (a) Dependence of the MSRE (training dataset) on the base thickness. (b),(c) Histograms of squared relative error for $d_p = 150$ μm and $d_p = 240$ μm . Red: $\text{DNN}_{\text{FeFeB}}$; blue: $\text{DNN}_{\text{FeFeB-Fe}}$.

depletion can be expressed as

$$f_p = \frac{1}{1 + \frac{N_V}{N_B} \exp\left(\frac{E_V - E_{FeI}}{kT}\right)}. \quad (12)$$

If N_B decreases, the level is filled with an electron, the SRH recombination ceases, and the ideality factor value sharply reduces — Fig. 2(a,b). Besides, a weak influence of impurities on ideality factor under low doping conditions is a reason for observed MSRE increase. In our opinion, the level filling is an additional reason for an error increase at high temperatures as well.

Fig. 7(a) shows that MSRE increases at both low and high iron concentrations. The first N_{Fe} area of bad DNN accuracy is entirely foreseeable, the second one is surprising enough. But according to Fig 7(c), the MSRE increasing at $N_{Fe} = 10^{13} \text{ cm}^{-3}$ is most likely determined by a few samples with big SRE value. Whereas SRE increasing is more systematic at $N_{Fe} = 10^{13} \text{ cm}^{-3}$ — Fig 7(b).

The ideality factor value for the case of interstitial iron only presence (n_{Fe}) gives additional information about defects in comparing with n_{Fe-FeB} . It is not surprising that $\text{DNN}_{\text{FeFeB-Fe}}$ has better operating parameters in comparing with $\text{DNN}_{\text{FeFeB}}$ — see Table 3, Table 4, Fig. 8. The operation improvement appearances in the MSRE decrease as well as in absence of huge difference between $N_{Fe, \text{TRUE}}$ and $N_{Fe, \text{PRED}}$ values and narrowing of SRE range (Figs. 4-8). Really, it is shown in Fig. 8 that the maximum SRE does not exceed one even in the case of All-varied datasets and SRE is less than 0.02 for 93%, 92%, 73%, and 97% of samples of T-varied, d-varied, B-varied, and Fe-varied datasets respectively. The R^2 (0.999) and R (0.999) values for Fe-varied dataset draws attention as well.

Despite the difference in predicting accuracy, $\text{DNN}_{\text{FeFeB-Fe}}$ features are similar to $\text{DNN}_{\text{FeFeB}}$ ones. Thus the DNN training with N_B values, which are expected in object of future research, is important for prediction accuracy (Fig. 8); the increase in the temperature value (Fig. 4) as well as decrease in doping level (Fig. 6) or iron concentration (Fig. 7) results in error rise. It should be noted that the prediction error gain with N_{Fe} increase not observed in $\text{DNN}_{\text{FeFeB-Fe}}$ case and SRE range at $N_{Fe} = 10^{13} \text{ cm}^{-3}$ is more narrow then those at $N_{Fe} = 10^{10} \text{ cm}^{-3}$ — see Fig. 7(b,c).

The results of training both $\text{DNN}_{\text{FeFeB}}$ and $\text{DNN}_{\text{FeFeB-Fe}}$ with full dataset are presented in Table 3, Fig. 3(f), and

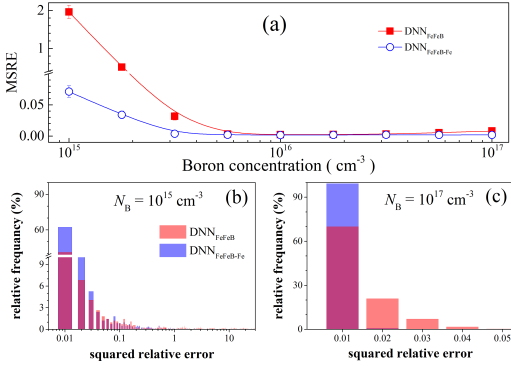


FIGURE 6 (a) Dependence of the MSRE (training dataset) on the boron concentration. (b),(c) Histograms of squared relative error for $N_B = 10^{15} \text{ cm}^{-3}$ and $N_B = 10^{17} \text{ cm}^{-3}$. Red: DNN_{FeFeB}; blue: DNN_{FeFeB-Fe}.

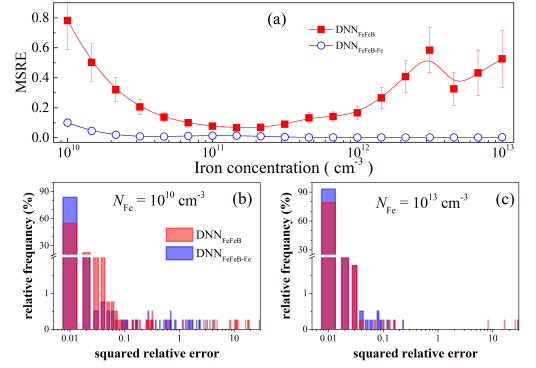


FIGURE 7 (a) Dependence of the MSRE (training dataset) on the iron concentration. (b),(c) Histograms of squared relative error for $N_{Fe} = 10^{10} \text{ cm}^{-3}$ and $N_{Fe} = 10^{13} \text{ cm}^{-3}$. Red: DNN_{FeFeB}; blue: DNN_{FeFeB-Fe}.

Fig. 8(f). One can see that the extension of the labeled dataset does not practically improve the DNN result in our case. In our opinion, there is evidence of i) a good DNN configuration tuning; ii) a limited predictive ability of DNN_{FeFeB}, which caused by ambiguity of dependence $n_{Fe-FeB} = f(N_{Fe})$.

4.2 | Experimental IV curves

The ability of DNNs to predict the iron concentration in real silicon SCs was tested as well. The n^+p-p^+ -Si samples were used in the experiment. The structures were fabricated from p -type boron doped Czochralski silicon wafer with [100] orientation and a resistivity of 10 Ohm·cm ($N_B = 1.4 \cdot 10^{15} \text{ cm}^{-3}$). The n^+ emitter with a surface resistance of about $(20 \div 30) \Omega/\square$ and a thickness of 0.7 μm was formed by phosphorus diffusion at 940°C. The anti-recombination isotype barrier was created by using p^+ layer $((10 \div 20) \Omega/\square, 0.6 \mu\text{m})$, which was formed by boron diffusion at 985°C. The base thickness was equal to 350 μm . The samples used in the experiment had the area of $1.52 \times 1.535 \text{ cm}^2$. The concentration of iron in the SC base $N_{Fe,MEAS}$ was determined from kinetic of the short circuit current under monochromatic illumination [52]. Two samples, referred to as SC320 and SC349 with $N_{Fe,MEAS}$ values of $(2.0 \pm 0.4) \cdot 10^{12} \text{ cm}^{-3}$ and $(6.7 \pm 0.7) \cdot 10^{12} \text{ cm}^{-3}$, respectively, were used in the investigation.

One can see that DNN was faced with a rather difficult task, in which complexity is associated with a certain mismatch between the parameters of real structures and those used in the simulation. However, the need for iron-related defects, which predominantly determine recombination, was the main criterion for sampling in our case.

The dark I - V characteristics of these samples were measured at temperatures of 300, 320, and 340 K. The measurements were taken after 48 h sample storage in the dark at room temperature ("Fe-FeB" case) as well as immediately after sample intense illumination with a halogen lamp ("Fe" case). After that, we used Eq. (10) to fit the experimental data and determine fitting parameters, in particular n , R_s , R_{sh} . The typical results of measurements and approximations are shown in Fig. 9 and Table 5. It should be noted that for real I - V curves, in contrast to synthetic ones, the influence of series and shunt resistances cannot be neglected (the R_s values are about 3 and 6 Ohm for samples SC320 and SC349, respectively, the R_{sh} values are listed in Table 5).

The values of the ideality factor, determined from the experimental curves, and the sample parameters were

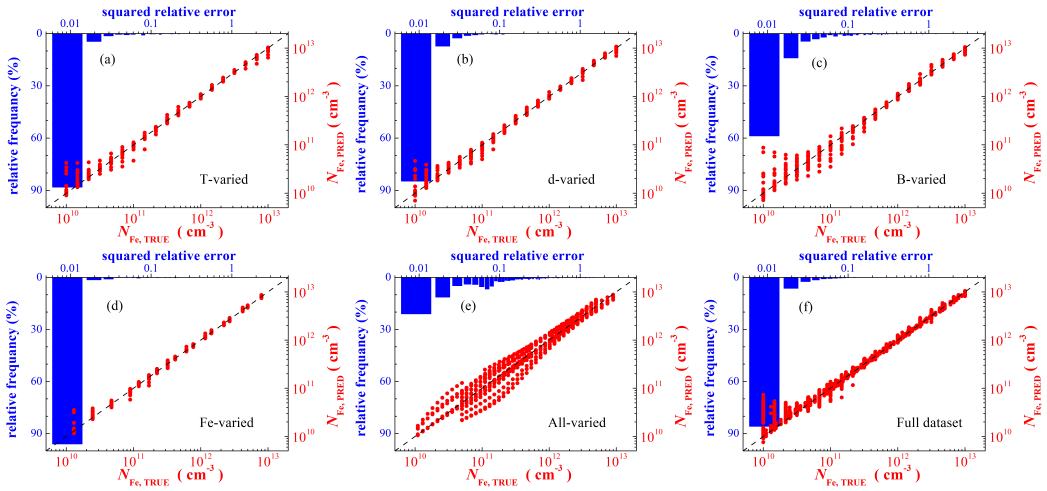


FIGURE 8 Iron concentrations are plotted against those generated by $\text{DNN}_{\text{FeFeB-Fe}}$ on T-varied (a), d-varied (b), B-varied (c), Fe-varied (d), All-varied (e), and full (f) datasets (red points). Bars represent histograms of squared relative error. DNN was learned by training (a)–(e) or full (f) dataset. The black dashed lines are the identify lines serving as the references.

used as input data for $\text{DNN}_{\text{FeFeB}}$ and $\text{DNN}_{\text{FeFeB-Fe}}$, which were trained on the training dataset or the full dataset. The predictions are listed in Table 5.

First of all, considering the not extreme high complexity of the simulation model, we note that the results even exceed expectations. Particularly for $\text{DNN}_{\text{FeFeB}}$, where the predicted iron concentrations differ by only several times from the measured ones. And in the case of sample SC320 and $\text{DNN}_{\text{FeFeB}}$, trained on the full dataset, the error does not exceed 40%.

Also, it should be noted that the results confirm the trends identified during analyzing synthetic I - V curves. Namely, the prediction accuracy decreases for $T > 320$ K and iron concentrations, which are close to the upper limit of the considered range (10^{13} cm^{-3}). These facts fully coincide with the data in Fig. 4a and Fig. 7a, respectively. In addition, the sample's base doping level ($N_B = 1.4 \cdot 10^{15} \text{ cm}^{-3}$) is not used in the training dataset but can be found in the d-varied dataset (see Supplementary Material). Table 5 shows that the prediction of $\text{DNN}_{\text{FeFeB}}$, trained by full dataset, is better than in the case of learning by training dataset only, especially for the SC320. This feature confirms the conclusion from the previous section about the importance of DNN training with N_B values, which are expected in the object of future research.

On the other hand, contrary to expectations, the $\text{DNN}_{\text{FeFeB-Fe}}$ demonstrate worse performance than $\text{DNN}_{\text{FeFeB}}$ in the case majority. There can be several reasons. Firstly, the use of two ideality factor values enhances the influence of simulation simplifications (e.g., the effect of unaccounted processes that cause the appearance of both shunt and series resistance). Secondly, the correct η_{Fe} determination is a more complicated experimental task than $\eta_{\text{Fe-FeB}}$ identifying. For example, it took about 100 s to obtain the I - V characteristics after intense illumination in our case. This interval consisted of time to set the temperature after illumination-induced heating as well as time to measurement. According to [53, 54], the characteristic association time of FeB pairs at $T = 340$ K and $N_B = 1.4 \cdot 10^{15} \text{ cm}^{-3}$ is about 600 s. Therefore, it cannot be expected that such a value of the ideality factor corresponds to the complete dissociation of FeB pairs. That is, despite the potentially higher accuracy of the $\text{DNN}_{\text{FeFeB-Fe}}$ predictions (shown in the previous section),

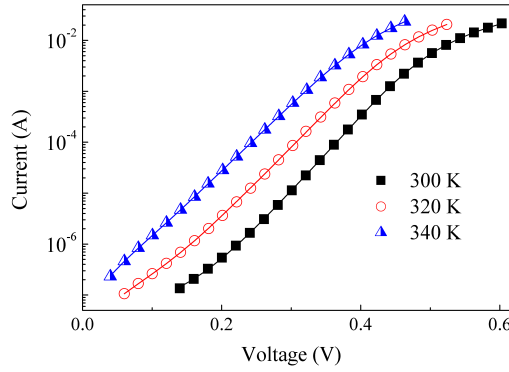


FIGURE 9 $I-V$ characteristics measured at 300 K, 320 K, and 340 K for sample SC320. The marks are the experimental results, and the solid lines are the curves fitted by Eq. (10).

TABLE 5 Results of experimental IV fitting and iron contamination testing

Sample	$N_{\text{Fe,MEAS}}, 10^{12} \text{ cm}^{-3}$	$T, \text{ K}$	$\eta_{\text{Fe-FeB}}$	$R_{sh,\text{Fe-FeB}}, \text{ Ohm}$	η_{Fe}	$R_{sh,\text{Fe}}, \text{ Ohm}$	$N_{\text{Fe,PRED}}, 10^{12} \text{ cm}^{-3}$			
							$\text{DNN}_{\text{FeFeB}}$		$\text{DNN}_{\text{FeFeB-Fe}}$	
							training	full	training	full
SC320	2.0 ± 0.4	300	1.214	$1.6 \cdot 10^6$	1.195	$1.4 \cdot 10^6$	3.9	2.8	3.0	2.0
		320	1.204	$8.6 \cdot 10^5$	1.148	$8.0 \cdot 10^5$	6.6	1.9	16	19
		340	1.118	$4.3 \cdot 10^5$	1.111	$4.3 \cdot 10^5$	3.8	1.2	89	574
SC349	6.7 ± 0.7	300	1.223	$2.9 \cdot 10^6$	1.222	$2.6 \cdot 10^6$	8.9	5.6	15	11
		320	1.183	$1.7 \cdot 10^6$	1.182	$1.7 \cdot 10^6$	1.2	0.4	10	32
		340	1.138	$1.3 \cdot 10^6$	1.173	$1.3 \cdot 10^6$	9.8	1.7	26	411

the practical application of this approach is more complex.

Generally, the results obtained for real SCs confirm the possibility of estimation for iron contamination by ideality factor value.

5 | CONCLUSION AND OUTLOOK

In this paper, we extracted the iron concentration in silicon BSF solar cells from an ideality factor value and systematically studied the performance of deep learning in this problem. This work is the first attempt at using deep learning for deep levels parameter retrieval from the current-voltage curve. In this model study, we used simulation to obtain training and test labeled datasets. Besides, a DNN was trial-tested by using the parameters of actual solar cells. Our results showed the ability of the deep neural network to predict iron concentration by using ideality factor values, SC base thickness and doping level, and temperature. MSRE was up to 0.005 for synthetic datasets. The simulation has shown the prospects for the use of two ideality factor values (for structure with Fe_i only as well as with Fe_iB_s and Fe_i coexistence) for upgrading a prediction accuracy. At the same time, the practical application of such an approach

manifested difficulties in obtaining correct data. It was important to train DNN with a boron concentration value, which agreed with the doping level of investigated structures. Moreover, the increase in iron concentration or boron concentration, as well as temperature decrease, results in a prediction error reduction.

The proposed approach envisages the utilization of a simple and widely applicable setup and does not require much time. Therefore it could be integrated into a manufacturing environment. However, it should be noted that we have simplified the task for our purposes. In our opinion, there are two ways of further improve the method. The first one connects with the refining of labeled datasets and can be realized by using 3D-simulators (e.g., SILVACO TCAD) or real IV measurements in a broad set of SCs. The improvement of DNN operation is the second one; and the fine-tuning is like most promising in this case. For example, not numerous input parameters can be multiplied and transformed to the picture and apply a vision model (e.g., VGG16).

ACKNOWLEDGMENTS

This work was supported by National Research Foundation of Ukraine (project number 2020.02/0036)

CONFLICT OF INTEREST

The authors declare that they have no known competing financial interests or personal relationships that could have appeared to influence the work reported in this paper.

DATA AVAILABILITY

The simulated IV characteristics, n_{Fe} and n_{Fe-FeB} values, and trained DNNs are available at <https://github.com/olegolikh/IVcharacteristics.git>.

REFERENCES

- [1] Claeys C, Simoen E. Metal Impurities in Silicon- and Germanium-Based Technologies: Origin, Characterization, Control, and Device Impact, vol. 270 of Springer Series in Materials Science. Berlin/New York: Springer International Publishing; 2018.
- [2] Zhu H, Yu X, Zhu X, Wu Y, He J, Vanhellemont J, et al. Low temperature iron gettering by grown-in defects in p-type Czochralski silicon. *Superlattices Microstruct* 2016 Nov;99:192–196.
- [3] Schmidt J. Effect of Dissociation of Iron–Boron Pairs in Crystalline Silicon on Solar Cell Properties. *Progress in Photovoltaics: Research and Applications* 2005 Jun;13(4):325–331.
- [4] Schubert MC, Padilla M, Michl B, Mundt L, Giesecke J, Hohl-Ebinger J, et al. Iron related solar cell instability: Imaging analysis and impact on cell performance. *Sol Energy Mater Sol Cells* 2015 Jul;138:96–101.
- [5] Schroder DK. *Semiconductor Material and Device Characterization*. Third ed. New Jersey: John Wiley & Sons; 2006.
- [6] Kurchin RC, Poindexter JR, Vähänissi V, Savin H, del Cañizo C, Buonassisi T. How Much Physics is in a Current-Voltage Curve? Inferring Defect Properties From Photovoltaic Device Measurements. *IEEE J Photovolt* 2020 Nov;10(6):1532–1537.
- [7] Peaker AR, Markevich VP, Coutinho J. Tutorial: Junction spectroscopy techniques and deep-level defects in semiconductors. *J Appl Phys* 2018;123(16):161559.

- [8] Bulyarskiy SV, Lakalin AV, Saurov MA, Gusarov GG. The effect of vacancy-impurity complexes in silicon on the current-voltage characteristics of p-n junctions. *J Appl Phys* 2020 Oct;128(15):155702.
- [9] Bulyarskiy SV. The effect of electron-phonon interaction on the formation of reverse currents of p-n-junctions of silicon-based power semiconductor devices. *Solid-State Electron* 2019 Oct;160:107624.
- [10] Claeys C, Simoen E. Device Performance as a Metrology Tool to Detect Metals in Silicon. *physica status solidi (a)* 2019 Sep;216(17):1900126.
- [11] Simoen E, Claeys C, Vanhellemont J. Defect Analysis in Semiconductor Materials Based on p-n Junction Diode Characteristics. In: *Defects and Diffusion in Semiconductors - An Annual Retrospective IX*, vol. 261 of *Defect and Diffusion Forum Trans Tech Publications Ltd*; 2007. p. 1–24.
- [12] Olikh OY. Relationship between the ideality factor and the iron concentration in silicon solar cells. *Superlattices Microstruct* 2019 Dec;136:106309.
- [13] van der Heide ASH, Schonecker A, Bultman JH, Sinke WC. Explanation of High Solar Cell Diode Factors by Nonuniform Contact Resistance. *Progress in Photovoltaics: Research and Applications* 2005 Jan;13(1):3–16.
- [14] Duan L, Yi H, Xu C, Upama MB, Mahmud MA, Wang D, et al. Relationship Between the Diode Ideality Factor and the Carrier Recombination Resistance in Organic Solar Cells. *IEEE Journal of Photovoltaics* 2018 Nov;8(6):1701–1709.
- [15] Chen J, Zhu M, Lu X, Zou X. Electrical characterization of GaN Schottky barrier diode at cryogenic temperatures. *Appl Phys Lett* 2020 Feb;116(6):062102.
- [16] Dalapati P, Manik NB, Basu AN. Analysis of the Temperature Dependence of Diode Ideality Factor in InGaN-Based UV-A Light-Emitting Diode. *Semiconductors* 2020 Oct;54(10):1284–1289.
- [17] Calado P, Burkitt D, Yao J, Troughton J, Watson TM, Carnie MJ, et al. Identifying Dominant Recombination Mechanisms in Perovskite Solar Cells by Measuring the Transient Ideality Factor. *Phys Rev Applied* 2019 Apr;11:044005.
- [18] Carleo G, Cirac I, Cranmer K, Daudet L, Schuld M, Tishby N, et al. Machine learning and the physical sciences. *Rev Mod Phys* 2019 Dec;91:045002.
- [19] Ju S, Shimizu S, Shiomi J. Designing thermal functional materials by coupling thermal transport calculations and machine learning. *J Appl Phys* 2020 Oct;128(16):161102.
- [20] Rodrigues S, Ramos HG, Morgado-Dias F. Machine learning PV system performance analyser. *Prog Photovoltaics Res Appl* 2018 Aug;26(8):675–687.
- [21] Ju S, Shimizu S, Shiomi J. Designing thermal functional materials by coupling thermal transport calculations and machine learning. *J Appl Phys* 2020 Oct;128(16):161102.
- [22] Jean J, Brown PR, Jaffe RL, Buonassisi T, Bulović V. Pathways for solar photovoltaics. *Energy Environ Sci* 2015 Jul;8(4):1200–1219.
- [23] Ajayan J, Nirmal D, Mohankumar P, Saravanan M, Jagadesh M, Arivazhagan L. A review of photovoltaic performance of organic/inorganic solar cells for future renewable and sustainable energy technologies. *Superlattices Microstruct* 2020 Jul;143:106549.
- [24] Green MA. Photovoltaic technology and visions for the future. *Prog Energy* 2019 Jul;1(1):013001.
- [25] Wilson GM, Al-Jassim M, Metzger WK, Glunz SW, Verlinden P, Xiong G, et al. The 2020 photovoltaic technologies roadmap. *J Phys D: Appl Phys* 2020 Sep;53(49):493001.
- [26] Burgelman M, Nollet P, Degraeve S. Modelling polycrystalline semiconductor solar cells. *Thin Solid Films* 2000 Feb;361–362:527–532.

-
- [27] Decock K, Khelifi S, Burgelman M. Modelling multivalent defects in thin film solar cells. *Thin Solid Films* 2011 Aug;519(21):7481–7484.
 - [28] Hu ET, Yue GQ, Zhang RJ, Zheng YX, Chen LY, Wang SY. Numerical simulations of multilevel impurity photovoltaic effect in the sulfur doped crystalline silicon. *Renewable Energy* 2015 May;77:442–446.
 - [29] Hamache A, Sengouga N, Meftah A, Henini M. Modeling the effect of 1 MeV electron irradiation on the performance of $n^+ - p - p^+$ silicon space solar cells. *Radiat Phys Chem* 2016 Jun;123:103–108.
 - [30] Kim K, Gwak J, Ahn SK, Eo YJ, Park JH, Cho JS, et al. Simulations of chalcopyrite/c-Si tandem cells using SCAPS-1D. *Sol Energy* 2017;145:52–58.
 - [31] Cappelletti MA, Casas GA, Cédola AP, y Blancá ELP, Soucase BM. Study of the reverse saturation current and series resistance of p-p-n perovskite solar cells using the single and double-diode models. *Superlattices Microstruct* 2018 Nov;123:338–348.
 - [32] Boubakeur M, Aissat A, Ben Arbia M, Maaref H, Vilcot JP. Enhancement of the efficiency of ultra-thin CIGS/Si structure for solar cell applications. *Superlattices Microstruct* 2020 Feb;138:106377.
 - [33] Casas GA, Cappelletti MA, Cédola AP, Soucase BM, Peltzer y Blancá EL. Analysis of the power conversion efficiency of perovskite solar cells with different materials as Hole-Transport Layer by numerical simulations. *Superlattices Microstruct* 2017;107:136–143.
 - [34] Pässler R. Dispersion-related description of temperature dependencies of band gaps in semiconductors. *Phys Rev B* 2002 Aug;66:085201.
 - [35] Yan D, Cuevas A. Empirical determination of the energy band gap narrowing in p^+ silicon heavily doped with boron. *J Appl Phys* 2014 Nov;116(19):194505.
 - [36] Green MA. Intrinsic concentration, effective densities of states, and effective mass in silicon. *J Appl Phys* 1990 Mar;67(6):2944–2954.
 - [37] Couderc R, Amara M, Lemiti M. Reassessment of the intrinsic carrier density temperature dependence in crystalline silicon. *J Appl Phys* 2014 Mar;115(9):093705.
 - [38] Klaassen DBM. A unified mobility model for device simulation – I. Model equations and concentration dependence. *Solid-State Electron* 1992 Jul;35(7):953–959.
 - [39] O'Mara WC, Herring RB, Hant LP. *Handbook of semiconductor silicon technology*. New Jersey, USA: Noyes Publications; 1990.
 - [40] Altermatt PP, Schmidt J, Heiser G, Aberle AG. Assessment and parameterisation of Coulomb-enhanced Auger recombination coefficients in lowly injected crystalline silicon. *J Appl Phys* 1997 Nov;82(10):4938–4944.
 - [41] Nguyen HT, Baker-Finch SC, Macdonald D. Temperature dependence of the radiative recombination coefficient in crystalline silicon from spectral photoluminescence. *Appl Phys Lett* 2014 Mar;104(11):112105.
 - [42] Murphy JD, Bothe K, Olmo M, Voronkov VV, Falster RJ. The effect of oxide precipitates on minority carrier lifetime in p-type silicon. *J Appl Phys* 2011 Sep;110(5):053713.
 - [43] Wijaranakula W. The Reaction Kinetics of Iron–Boron Pair Formation and Dissociation in P-Type Silicon. *J Electrochem Soc* 1993 Jan;140(1):275–281.
 - [44] Zoth G, Bergholz W. A fast, preperetion-free method to detect iron in silicon. *J Appl Phys* 1990 Jun;67(11):6764–6771.
 - [45] Geerligs LJ, Macdonald D. Dynamics of light-induced FeB pair dissociation in crystalline silicon. *Appl Phys Lett* 2004 Nov;85(22):5227–5229.

-
- [46] Rougieux FE, Sun C, Macdonald D. Determining the charge states and capture mechanisms of defects in silicon through accurate recombination analyses: A review. *Sol Energy Mater Sol Cells* 2018 Dec;187:263 – 272.
 - [47] Istratov AA, Hieslmair H, Weber ER. Iron and its complexes in silicon. *Applied Physics A: Materials Science & Processing* 1999 Jul;69(1):13–44.
 - [48] Breitenstein O. Understanding the current-voltage characteristics of industrial crystalline silicon solar cells by considering inhomogeneous current distributions. *Opto–Electronics Review* 2013 Sep;21(3):259–282.
 - [49] Yu K, Liang JJ, Qu BY, Chen X, Wang H. Parameters identification of photovoltaic models using an improved JAYA optimization algorithm. *Energy Conversion and Management* 2017 Oct;150:742–753.
 - [50] Olikh OY, Zavhorodnii OV. Modeling of ideality factor value in $n^+ - p - p^+ - \text{Si}$ structure. *Journal of Physical Studies* 2020;24(4):4701.
 - [51] Chollet F. *Deep Learning with Python*. Second ed. Manning; 2017.
 - [52] Olikh O, Kostylyov V, Vlasuk V, Korkishko R. Estimation of Iron Concentration in Silicon Solar Cell by Kinetics of Light-Induced Change in Short-Circuit Current. In: *II International Advanced Study Conference Condensed Matter and Low Temperature Physics CM<P 2021*. Book of Abstracts. Kharkiv, Ukraine. Kharkiv; 2021. p. 191.
 - [53] Möller C, Bartel T, Gibaja F, Lauer K. Iron-boron pairing kinetics in illuminated p-type and in boron/phosphorus co-doped n-type silicon. *J Appl Phys* 2014 Jul;116(2):024503.
 - [54] Khelifati N, Laine HS, Vähäniemi V, Savin H, Bouamama FZ, Bouhafs D. Dissociation and Formation Kinetics of Iron–Boron Pairs in Silicon after Phosphorus Implantation Gettering. *Phys Status Solidi A* 2019 Sep;216(17):1900253.